Arctic Sea Ice During the Winter to Summer Transition as seen by the AMI-Wind and ATSR/M of ERS-1

Robert Ezraty, Francis Gohin and Alain Cavanié

IFREMER/Centre de Brest – Département d'Océanographie Spatiale
B.P. 70, 29280 Plouzané – FRANCE
Tel : (33) 98 22 42 99 – Fax : (33) 98 22 45 33

ABSTRACT

The Active Microwave Instrument-Wind (AMI-Wind), which is the C-Band scatterometer of ERS-1 was primarily designed to measure the wind vector over the world oceans. The Along-Track Scanning Microwave Radiometer (ATSR/M) was included in the ERS-1 payload to provide the atmospheric corrections needed for accurate sea-level measurements by the Radar Altimeter.

Because of the near-polar orbit of ERS-1, both instruments are able to sense large areas of Arctic and Antarctic. In this paper, the complementarity of scatterometer and ATSR/M data over sea-ice is discussed. Its is shown that the information from both sensors is highly correlated whatever the season although during winter, the scatterometer provides a more detailed mapping of sea-ice than does the ATSR/M, while the latter better delineates the transition from open ocean to ice. During summer, it is well known that melting of sea-ice and its snow cover produces ponds which changes the electromagnetic properties of the surface; this hampers interpretation of the microwave measurements for both passive and active instruments. In late summer or early winter, backscattering over sea-ice evolves rapidly towards its typical winter-time signature.

INTRODUCTION

Numerous studies have been devoted to microwave remote sensing of sea-ice and its geophysical applications. The reader is referred to a recent monograph (Editor F.D. Carsey, 1992) for an updated and comprehensive review of both passive and active sensor signatures over sea-ice, the underlying physical principles, modeling and applications.

Passive microwave instruments such as the Scanning Multichannel Microwave Radiometer, SMMR, and the Special Sensor Microwave Imager, SSM/I, have been and are still routinely used to estimate sea-ice types, sea-ice extent and ice concentration. Because of their wide swath, these instruments are certainly more suited for ice mapping than the Along Track Scanning Radiometer/Microwave, ATSR/M, which operates at similar frequencies but is limited to a sub-satellite footprint.

Synthetic Aperture Radars, SAR, are presently the active sensors favoured by the sea-ice research community because they provide very detailed, high resolution information. The drawback is that the amount of data and the specific processing restrict their use to limited areas and short periods of time unless enormous expenses are accepted.

Since SASS (SEASAT A Scatterometer Sensor) and, for example, the studies by Carsey (1985), satellite scatterometry has been given little attention due to the lack of data. The launch of ERS-1 with its Active Microwave Instrument has renewed the interest in sea-ice scatterometry not only for validation of wind vector data in the vicinity of the ice canopy but also as a subject in itself because of its potential applications in monitoring sea-ice extent and types. Moreover, follow-on satellite missions, ERS-2, NSCATT and the Polar Platform will fly scatterometers ensuring long-term data continuity of importance for climatological applications.

Since the accurate engineering calibration of ERS-1 scatterometer and the latest tuning of the processing algorithms in early February 1992, normalized radar cross section (σ^0) are now routinely available.

Recently, Cavanié and Gohin (1992, 1993) have shown how the ERS-1 scatterometer can be used to map sea-ice provided an incidence angle correction is applied. On such maps, discrimination between first and multi-year ice is possible, because of their different backscatter signatures.

The goal of this study is to evaluate the observed scatterometer signatures against now well-accepted passive microwave observations, to ascertain advantages, drawbacks and possible complementarity.

The first section of this paper recalls the main characteristics of the scatterometer and those of the ATSR/M relevant to sea-ice studies. The second section presents the data set used and the processing performed, and the third one gives the combined analysis of both signals followed by a discussion and conclusions.

1. ERS-1 SENSORS FOR SEA-ICE STUDIES

1.1 The AMI-Wind

The AMI-wind is a three beam C-band scatterometer, VV polarized, which operates at 5.3 GHz. The swath is 500 km wide, starting 250 km to the right of the ground track. Incidence angles of the electromagnetic beams vary from 25 to 59 degrees for the forward and rear antennae and from 18 to 47 degrees for the central one. The swath is divided into 19 cells of size 25 by 25 km. Since ERS-1 is yaw-steered, the forward and rear beams have the same incidence angles to better than 0.1 degree. A description of scatterometer geometry can be found in Louet (1986).

Using the assumption that sea-ice is isotropic, Cavanié and Gohin (1992) have shown that, over sea-ice, the normalized radar cross section (σ^0), of the forward and rear beam are identical, at the same incidence angle, within the noise level limits (6 % of measured value). An anisotropy index is defined as :

$$A = (\sigma^0_1 - \sigma^0_3)/(\sigma^0_1 + \sigma^0_3)$$

where indices 1 and 3 represent the forward and aft beam respectively. Values of A randomly distributed about zero and less than 0.05, indicate a sea-ice target.

Given the redundancy of incidence angle provided by the central beam, Gohin and Cavanié (1993) developed an incidence angle correction which permits mapping of the σ^0 at the nominal incidence angle of 40 degrees. This correction relies on the linear relationship, observed over the Arctic, between σ^0 (in dB) and the incident angle. These maps clearly exhibit geophysical signatures related to first and multi-year sea-ice over both polar caps.

The orbit inclination of ERS-1 is 98.5 deg. Given the width of the scatterometer swath and its location to the right of the ground tracks, areas located up to 87.8 degrees North can be remotely sensed. At these latitudes, the polar region is nearly completely mapped every 3 days of a 35 day repeat orbit cycle.

The Scatterometer and the Synthetic Aperture Radar (SAR in image mode) are the two combined instruments of the Active Microwave Instrument of ERS-1. They share common hardware components, thus they cannot be operated simultaneously. Since the ice program with SAR has a higher priority in the North Canadian area than the scatterometer data acquisition program, data gaps do occur for the latter and presently prevent monitoring of the complete ice canopy with this sensor.

1.2 The ATSR/M

The ATSR/M is a near nadir-looking radiometer which operates at two frequencies : 23.8 and 36.5 GHz. The field of view (FOV) of the forward beam (36.5 GHz) is an ellipsoid whose axes are 21.7 and 18.5 km, the FOV of the rear beam can be approximated by a 20 km radius circle. The center of the 36.5 GHz FOV is located 34 km ahead of the nadir of the satellite while the 23.8 GHz FOV is located 26.1 km behind. A full description of the ATSR/M, its calibration and validation can be found in Eymard *et al.* (1993). The estimated accuracy of the measured brightness temperatures is 3 K. Since the ATSR/M senses along track, the highest latitudes reached are 81.5 deg. North and South.

2. THE DATA SET

Scatterometer and ATSR/M data are extracted from the French-PAF (Processing and Archiving Facility), called the CERSAT (Centre ERS d'archivage et de Traitement). The period of the present study starts on 14 April 1992 which corresponds to the beginning of the 35 day repeat cycle of ERS-1. Since then, ATSR/M data are systematically processed for the purpose of sea level altimeter corrections.

It is also important to recall that the final tuning of the σ^0 processing at the receiving stations occurred in late February 1992, *i.e.* before the beginning of this data set.

2.1 Scatterometer data

σ^0 scatterometer values are obtained from the Fast Delivery Products data sets produced in near real time at the ESA receiving stations and archived at CERSAT.

For this study, average maps of σ_0, using the three beams at the nominal incidence angle of 40 deg. have been compiled, onto the polar stereographic grid used by the National Snow and Ice Data Center (NSIDC), limited to 48 deg. North. The pixel size is 25 by 25 km, with a dynamic of 253 levels for σ^0 values from 1/1500 to 253/1500. Zero corresponds to no data (either missing or two beam scatterometer operations or erroneous data). The value 254 codes water detection using the scatterometer sea-ice algorithm and 255 represents land.

Figure 1 presents a map of σ^0 at 40 deg. incidence angle over the North polar region. Because no significant variations in σ^0 could be detected in the maps obtained for early April and on a three day basis during these 10 days, this map is a pixel by pixel average of all scatterometer data after the incidence angle correction had been applied. The number of samples per pixel varies from 1 to 40 with an average value of 5. The larger number of samples per pixel occur at high latitudes, above 85° N.

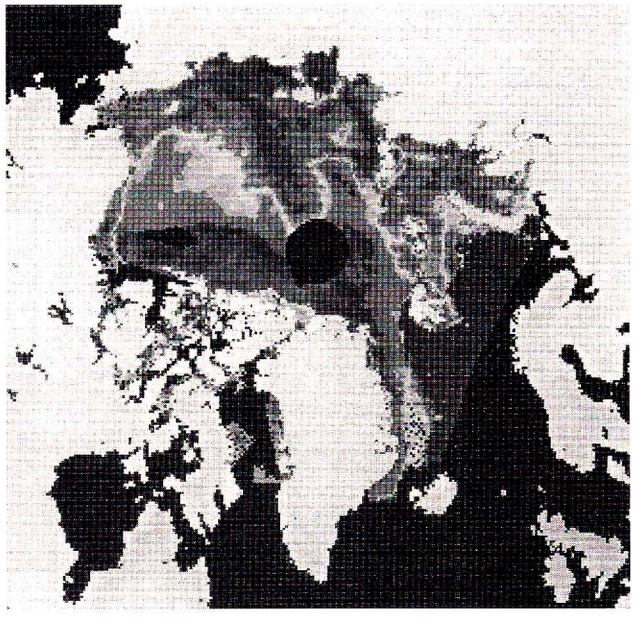

Fig. 1 - Map of Scatterometer backscatter at 40 degree incidence angle for the period April 14-23, 1992

Dark blue represents either no data due to SAR operation, for example in the Canadian area, or data outside the area of interest or no scatterometer coverage (the circle around the North pole). Areas where open-water is detected, within the area of interest, are coded in brown.

High values of backscatter, in yellow and red shades, corresponding to multi-year ice, are mainly concentrated along North Greenland and the North Canadian coast. Intermediate values of σ^0 are coded in green while low backscatter, corresponding to smooth young ice is coded in blue. The color coding enhances transitions and eases the identification of some geophysical features, for example the tongue of ice of intermediate backscatter along 120° E. penetrating into the low backscattering ice of the Siberian area. These regions of transition will be used to compare the response of the scatterometer and that of the ATSR/M over identical targets.

2.2 ATSR/M data

ATSR/M data are processed off-line at CERSAT. The individual radiometric counts (every 150 ms) are converted to brightness temperatures (T_b), averaged over 1.2 s and the data of both channels are collocated at the nadir of the satellite. It is this averaged value which is used here for comparisons with the scatterometer while the standard deviation of the individual counts will be used for the validation of ice concentration estimations.

For the purpose of collocation with the scatterometer σ^0, the T_b of each orbit and each channel are mapped on the reduced NSIDC grid with the same pixel size of 25 by 25 km. Before mapping, the ATSR/M data are controlled according the procedures described by Ezraty (1992). The land mask flag included at CERSAT processing level is not used here. The same NSIDC land mask used to map the scatterometer data is employed.

Since this study focuses on the comparison of ATSR/M and scatterometer data over sea-ice, a lower limit of 150 K was set under which T_b are discarded for both channels. This lower limit mostly affects the 23.8 GHz channel over water. An example of sea-ice to water transition using both instruments and the full T_b range for ice concentration estimation will be presented later.

The T_b maps are coded on a 8 bit scale so that the coded value, V, is :

$$V = 1.5*(T_b-150)$$

The value zero corresponds either to no data or to $T_b \leq 150$ K and the value 255 is reserved to code land as in the scatterometer case. Open-water T_b's are over 150 K at 36.5 GHz, while at 23.8 GHz, they are of the order of 140 K. Over sea-ice, T_b's are above 200 K. Because this

study focuses on the comparison of signatures over sea-ice, the lower limit of 150 K was selected to expand as much as possible the dynamic of the images; the image of the 36.5 GHz channel still allowing discrimination of open-water.

Observing the T_b values from neighboring ground tracks, using the 3 day orbit sub-cycle, significant changes in brightness temperatures were noticed (more than 15 K during the reference period). Due to the narrow FOV of the sensor, it was not possible, to compile a meaningful pseudo map of brightness temperatures for the ATSR/M, as available, for example, with the SSM/I for shorter periods.

To perform quantitative comparisons between the signatures of the scatterometer and of the ATSR/M, five ground tracks have been selected which sample the polar cap either along Siberia or between Canada and Siberia. These ground tracks and the brightness temperatures of the 23.8 GHz channel are plotted in Figure 2 for the period April 14-23. Table 1 presents the dates of the orbit segments and starting locations used either for comparisons during this reference period or until December 1992.

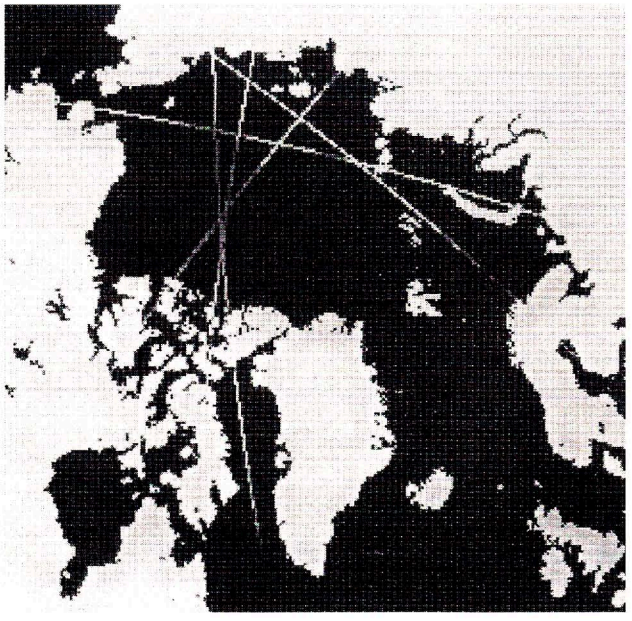

Fig. 2 - Map of the ATSR/M ground tracks used in the analysis. To ease identification of T_b values, the FOV of the sensor has been magnified and is not to scale

Table 1 - Identifications of Orbits

Orbit #	Start time (1992) MM/DD HH:MM:SS	Start location Lat - Long
3902 *	04/14 08:30:27	69.19 - 189.83
4403 *	05/19 08:15:10	"
4904 *	06/23 08:15:19	"
5405 *	07/28 08:15:25	"
5906 *	09/01 08:15:24	"
6407 *	10/06 08:15:23	"
6908 *	11/10 08:15:20	"
7409 *	12/15 08:15:09	"
3903	04/14 09:55:44	69.91 - 163.15
3912	04/15 01:16:25	76.52 - 282.53
3928	04/16 03:50:50	77.20 - 236.92
4027	04/23 01:49:58	76.02 - 271.99

The * indicates the orbits with identical ground tracks (every 501 revolution)

3. JOINT ANALYSIS OF SCATTEROMETER AND ATSR/M DATA

The purpose of the joint analysis of the three cases presented here is to compare :

i) the dynamics of scatterometer and ATSR/M signals over identical sea-ice features,
ii) the response of both instruments at a sea-ice to open-water transition,
iii) the time stability of σ^0 compared to brightness temperatures, except in the summer period when the signals of both sensors are hampered by melting.

3.1 Sigma-zero and brightness temperature dynamics

The brightness temperatures along the ground tracks of orbits 3912, 3928 and 4027 (from Northern Canada to Siberia) have been selected for comparison with the σ^0, at the same locations and for the period April 14-23, because of their wide range of variations.

Table 2 presents the main statistics (mean, standard deviation, maximum and minimum values) for each of these orbits and signals. From these figures, it may be anticipated that the areas sensed by the 3 orbits are similar. The parameter R is defined later in this chapter.

Table 2 - Statistics of Orbit # 3912, 4027 and 3928

	Orbit	3912	4027	3928
$T_{b,23}$	Mean	225.2	229.3	228.5
(K)	Std	13.5	15.5	13.4
	Max	245.3	250.6	247.3
	Min	200.6	201.3	205.3
	R	14.9	16.4	14.0
$T_{b,36}$	Mean	218.9	222.2	222.3
(K)	Std	20.4	21.7	18.7
	Max	250.0	252.6	250.6
	Min	180.6	181.3	190.6
	R	23.1	23.7	20.0
σ^0	Mean	4.28	4.14	3.96
$*10^2$	Std	2.45	2.59	2.42
	Max	9.20	8.87	9.07
	Min	0.73	0.73	1.20
	R	33.0	32.8	33.0

See text for the definition of R

Figure 3 presents, for the three orbits, the normalized values of both T_b and - σ^0 (the justification of the minus sign will be discussed later) along each ground track. For each orbit, both parameters are centered about their mean values and divided by their standard deviation.

All three orbits exhibit the same trend for the three signals. Moreover at each orbit the variations of $-\sigma^0$ are closely related to the variations of Tb indicating, on the average, a good correlation.

For both channels of the ATSR/M, the estimated accuracy,a, is 3 K (Eymard *et al.*, 1992). For the scatterometer, a is 6% of the measured value and, for this application, the mean σ^0 value of each orbit is used.

To quantify and compare the dynamics of the signals, the ratio, R, of the maximum variation to the accuracy, a, is used :

R = (Max-Min)/a.

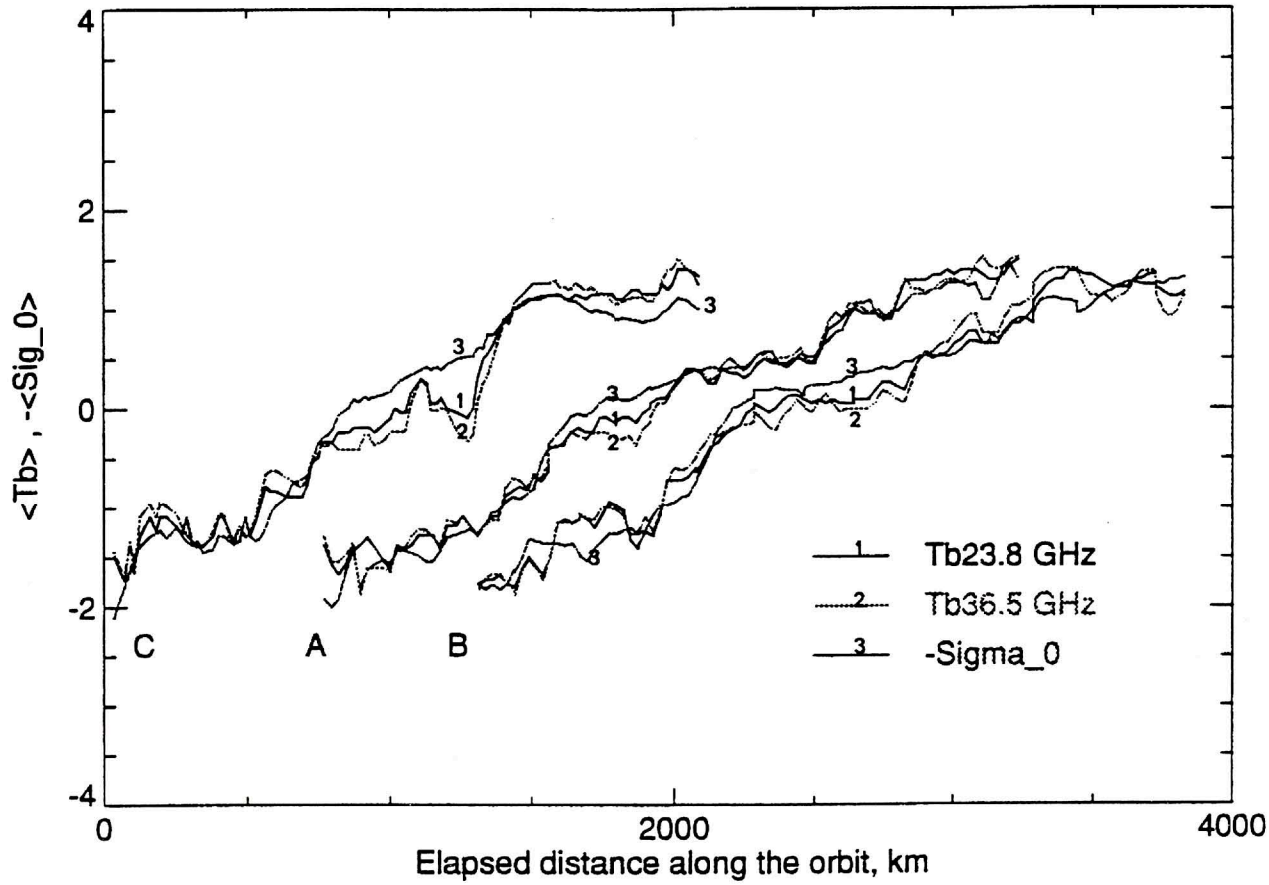

Fig. 3 - Dimensionless plots of brightness temperatures (<T_b>) and σ^0 (<Sigσ0>) for orbits # 3912 (A), 4027 (B) and 3928 (C) as a function of the relative distance from a reference location on each ground track. See text for definitions of <T_b> and <Sigσ0>

Comparing the values of R (Table 2), obtained for the 23.8 GHz with the values of the 36.5 GHz channel (resp. about 15 and 22) confirms that the latter has more dynamic over sea-ice than the former. It interesting to note that this ratio reaches about 33 for the scatterometer, indicating that this sensor should be more sensitive over sea-ice than the ATSR/M.

3.2 ATSR/M and scatterometer at a sea-ice to open-water boundary.

Orbit 3903 was selected to illustrate the behavior of both sensors at sea-ice to open-water transition. The ground track goes from East Siberia to Northern Norway. As can be seen in Figure 2, the transition is located about 78° N and 50° E.

Figure 4 presents three quantities as a function of distance along the ground track : The scatterometer anisotropy index, A, as defined in chapter I-1, σ^0 in the form of the dimensionless parameter : $S_n = 1-(\sigma^0/\sigma^0_{max})$, where σ^0_{max} = 253/1500, and the T_b of the 36.5 GHz channel in the dimensionless form: $T_n = (T_b-160)/(270-160)$.

The scatterometer signal is weak all along the ground track and fluctuates about 0.0168 except for 4 spikes at km 1700, 2100, 2350 and 2600 which are due to contaminations from ice covered islands (near Severnaya Zemlya and Franz Joseph Land). From km 2900 to 3100 a large fluctuation occurs which is not related to a particular land location followed by an area where the signal approximately reaches its previous level.

The anisotropy index randomly fluctuates around zero (0.2 was added to facilitate visualization on the graph) up to km 3000. The level of fluctuations increases by a factor of two at km 3000 over about 400 km and then regularly increases up to 0.5, indicating that the last 400 km are open-water.

The sudden sharp decrease from 250 K to 160 K, at km 2900, of the 36.5 GHz brightness temperature (the 23.8 GHz channel, not shown here, has the same behavior),

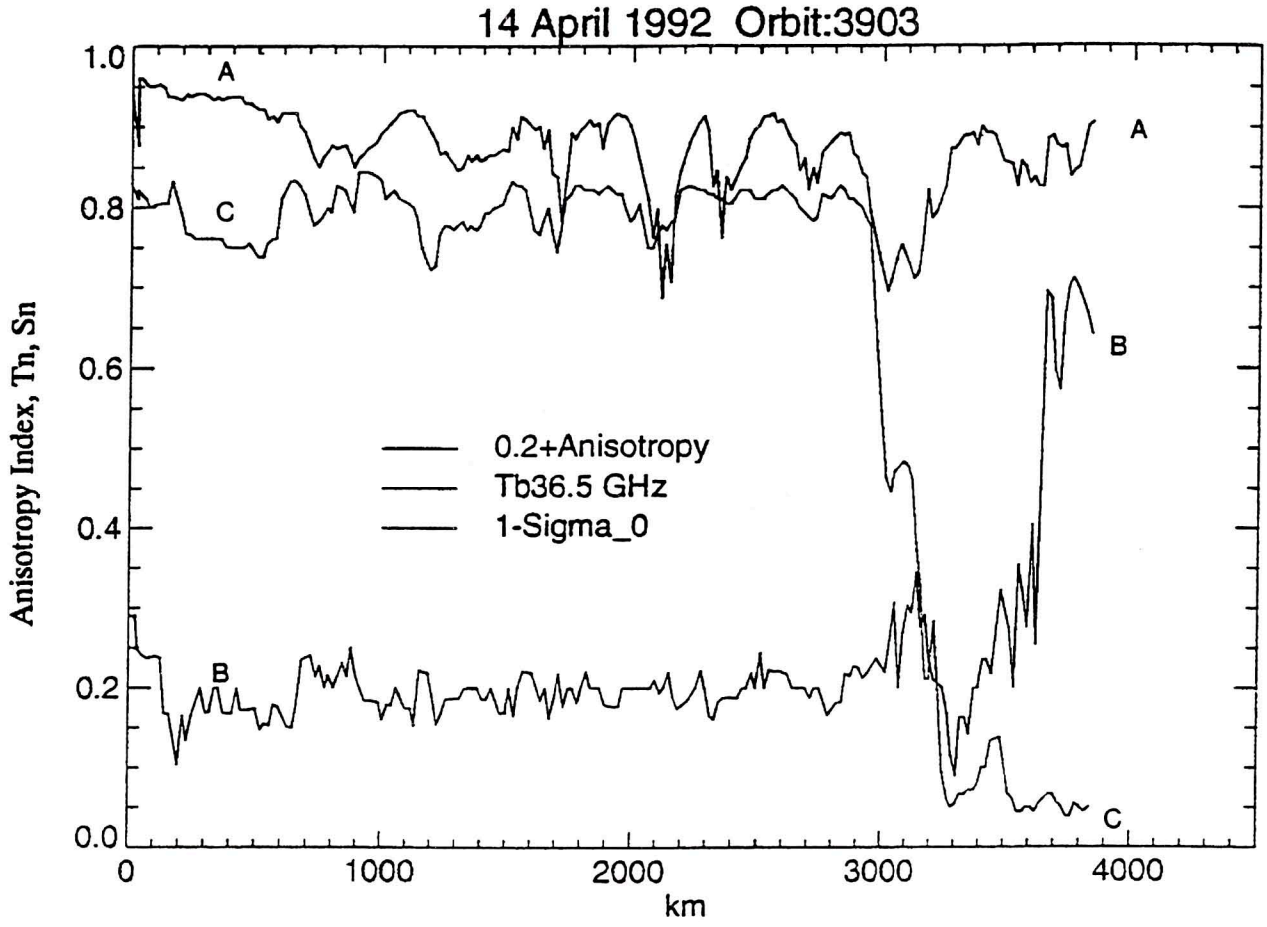

Fig. 4 - Illustration of a sea-ice to open-water transition. Dimensionless plot of σ^0 (A), anisotropy index (B) and 36.5 GHz brightness temperature (C) along the ground track of orbit # 3903. See text for definitions of T_n and S_n

facilitates the detection of the sea-ice to open-water boundary limited to about 300 km. Thus it seems unlikely to be able to estimate ice concentration from the scatterometer signals in contrast to the ATSR/M data.

To estimate ice concentration, the frequency diagram of the Comiso-Sullivan method (Comiso and Sullivan, 1986) has been adapted to the 23.8 and 36.5 GHz channels. Since ATSR/M is a near-nadir (VV polarized only) instrument, the polarization information is not available. The algorithm, developed over Antarctica (Ezraty, 1993), relies on locally selected ocean tie points. The likelihood of ice concentration estimations is primarily constrained by the standard deviation of the elementary brightness temperature measurements every 150 ms, because the standard deviation depends on the variations of levels rather than on the levels themselves.

Figure 5 presents, for the second half of orbit 3903 from km 2000 to 4000, the brightness temperatures, the standard deviation of elementary measurements for both channels and the sea-ice concentration estimate.

Figure 5a clearly indicates that the temperatures drop from 250 K down to 130 K in two steps located at km 3050 and 3150. At km 3500, atmospheric attenuation affects both brightness temperatures. According Eymard *et al.* (1992), the T_b variations at km 3500 correspond to a water vapor variation from 0.045 g/cm^2 to 0.3 g/cm^2.

In Figure 5b, the presence of sharp spikes confirms the position of the transition area but also indicates the area of important atmospheric effect. Note also that the level of fluctuations over sea-ice is about 3 to 4 times the level over ocean. Three physical effects adding together explain this ratio : first, the ratio of sea-ice to open-water emissivities is about two, thus the fluctuations of T_b vary accordingly, second sea-ice being an heterogeneous medium its emissivity fluctuates more than that of open-water and third within the FOV of the instrument the ocean surface temperature is more uniform than that of sea-ice.

Figure 5c is an example of the limits of the present automatic validation algorithm of ice concentration results. In the open-water area, at km 3500, an atmospheric attenuation induces a 10% ice concentration artifact. Also, within the marginal zone, an area of the size of one footprint is detected as open ocean, and might be likely, although a 20% ice concentration seems a realistic value observing the continuity of T_b values at neighboring locations.

3.3 Time evolution of scatterometer and ATSR/M signatures along a ground track

The ground track of orbit 3902 from Bering Strait to Severnaya Zemlya has been selected as a representative sample to follow the time evolution of scatterometer and ATSR/M signatures over sea-ice since a continuous data set was available from April to December for both sensors. This ground track samples also the southern tip of an ice area of high backscattering, along 120° E.

To facilitate visualization, Figure 6a and 6b show σ^0 (the plotted value is - σ^0) and the 36.5 GHz brightness temperatures as a function of the elapsed distance along the ground track, from East to West. Each of these figures have been split into three frames corresponding to the end of the winter period and the beginning of spring (April and May, orbits 3902 and 4403), the summer period (late June until 1st September, orbits 4904, 5405 and 5906) and the fall (October, November and December, orbits 6407, 6908 and 7409).

At the end of the winter period, the σ^0 signatures remain stable (upper frame of Figure 6a), except for a displacement of the high backscattering region, around km 2000, 100 km to the East. For the same period, the brightness temperatures (upper frame of figure 6b) have clearly shifted to higher values. Moreover, the lower emissivity area is smeared and its variation is not as evident as on the scatterometer signal. The mean and the standard deviation of the three signals for the two orbits are presented in Table 3. It can be seen that the average brightness temperatures have increased by 13 and 15 K while the mean σ^0 has not significantly changed although it was shown in chapter 3.1 that the scatterometer signal had a larger dynamic range than that of the ATSR/M. The standard deviation of the three signals does not change significantly from April to May, indicating the same global variability for the two periods.

Table 3 - Comparison of Orbit 3902 and 4403

	Orbit	3902	4403
$T_{b,23}$	Mean	236.5	249.9
(K)	Std	4.9	5.5
$T_{b,36}$	Mean	237.4	253.0
(K)	Std	6.9	7.1
σ^0	Mean	2.47	2.48
$*10^2$	Std	0.91	0.93

To emphasize this behavior, each of the scatterometer and ATSR/M signals have been centered and normalized by the mean and standard deviations of the April signatures and

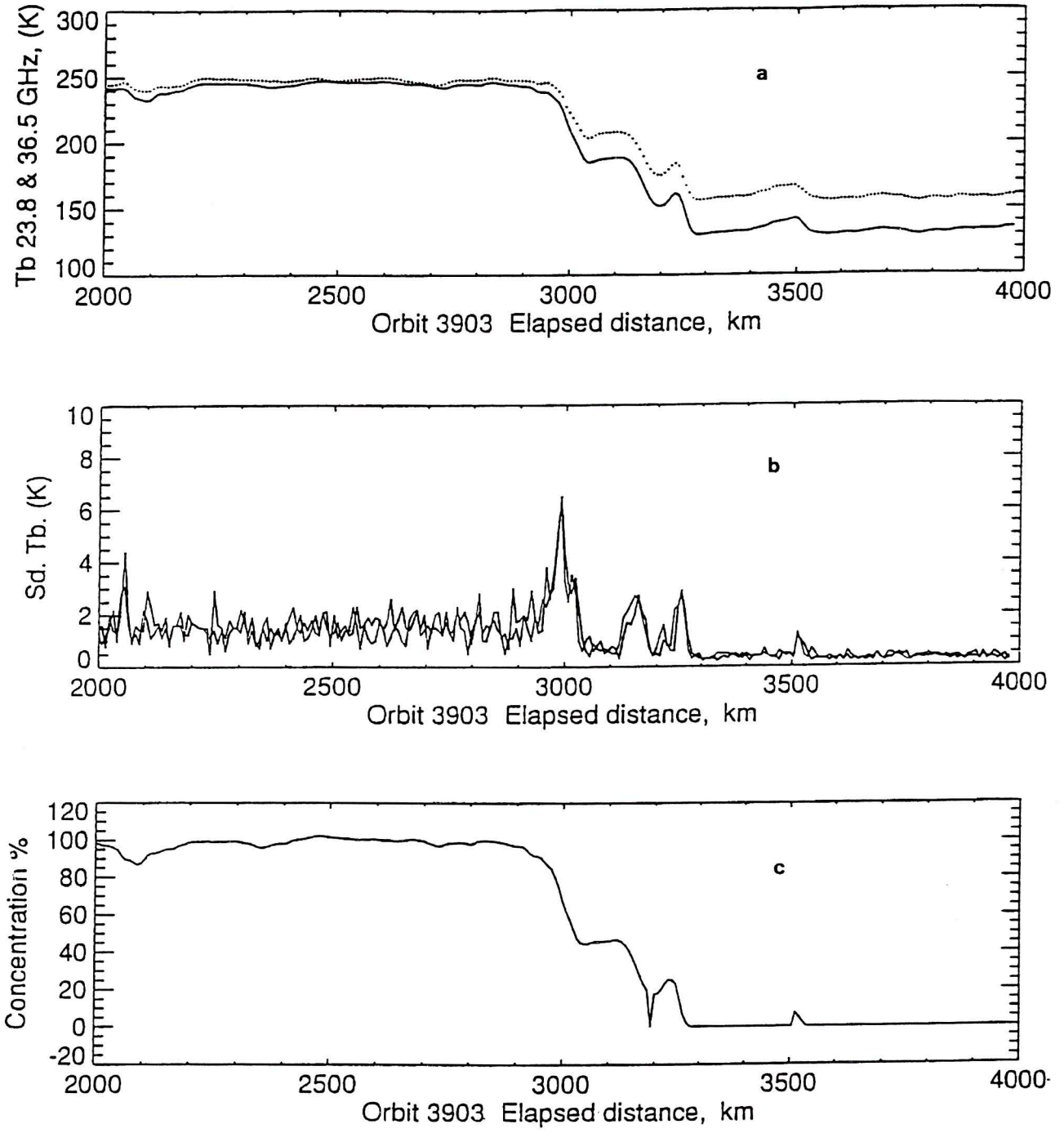

Fig. 5 - Sea-ice concentration estimate from ATSR/M data on April 14, 1992.
a) Brightness temperature, full line 23.8 GHz, dotted line 36.5 GHz,
b) Standard deviation of elementary brightness temperature measurements,
c) Ice concentration results

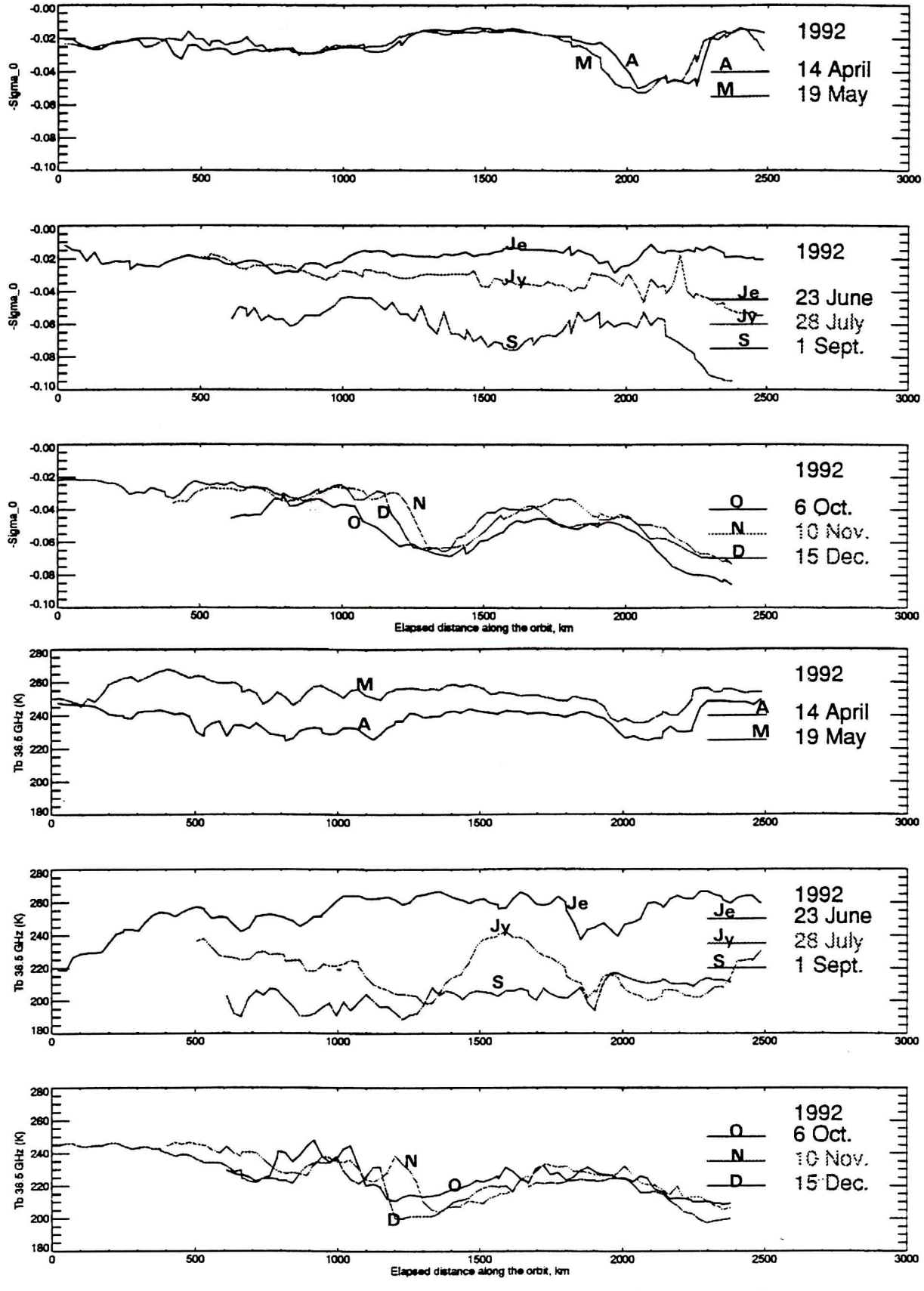

Fig. 6a - Time evolution of scatterometer signatures along the ground track of orbit # 3902 from April to December 1992. - σ^0 at 40 degree incidence angles

Fig. 6b - Time evolution of ATSR/M signatures along the ground track of orbit # 3902 from April to December 1992. 36.5 GHz brightness temperatures

the differences are presented in Figure 7 as a function of distance. It can be seen that the scatterometer remains stable (oscillations about zero) all along the ground track except for the two spikes corresponding to the displacement of the ice feature previously identified. The changes in brightness temperature are not uniform and relatively much more important since they vary as a function of longitude from about 35 K in the Eastern part of the ground track to 10 K in the Western part. Moreover, only the displacement of the Western edge of the canopy is clearly identified while the Eastern edge is buried into the fluctuations.

The middle frames of figures 6a and 6b show the large variations in σ^0 and T_b during the summer period. Although for the scatterometer the signature along the Eastern part of the ground track for June data is very similar to the May and April values, the signature of the Western part is totally different. As expected, the brightness temperatures do differ, even at the Eastern locations.

Because of melting, the physical and electromagnetic properties of the upper layers of the ice are modified, which induces large changes in both emissivity and backscattering. From end of June to beginning of September, the occurrence of water particles, as surface temperature likely increases with air temperature, tends to lower the Tb and increase backscattering (the plotted value is - σ^0).

The lower frames of Figures 6a and 6b present the new situation which appears in autumn. As surface temperatures decrease from October to November, this situation tends to approach the December signature. Backscatter decreases and both σ^0 and T_b show identical signatures (note the same dip around km 1400) in October and November as was observed in late winter. Note also that both sensors indicate the same displacement of the Eastern edge of this dip from East to West for the first two months and from West to East in December.

4. DISCUSSION

The AMI-Wind and the ATSR/M of ERS-1 provide a new opportunity to carry out comparative and synergetic stu-

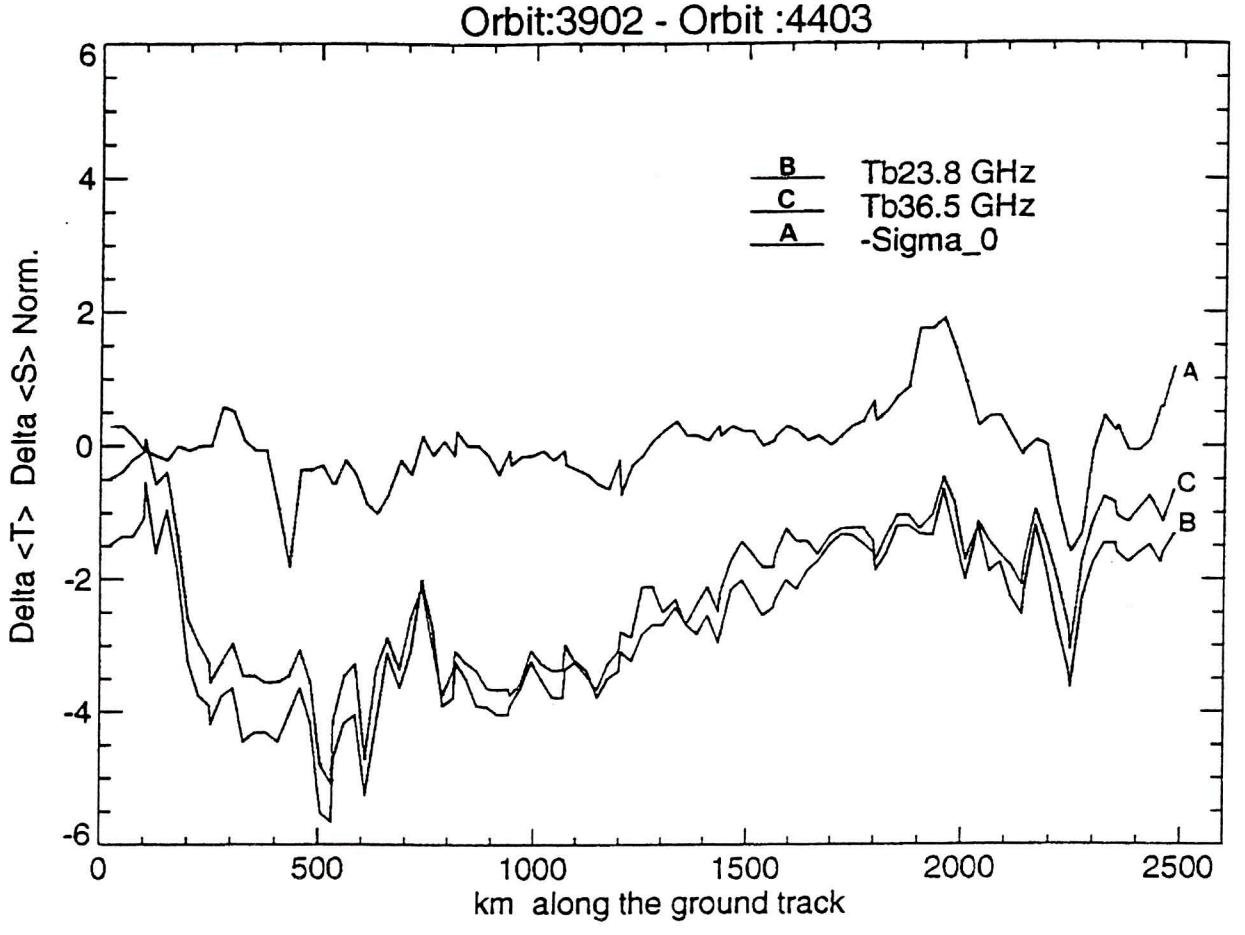

Fig. 7 - Comparison of scatterometer and ATSR/M signatures, late winter. Difference of normalized signatures between April and May 1992 along the same ground track. -σ^0 (A), 23.8 GHz (B) and 36.5 GHz (C) brightness temperature

dies of the signatures of active and passive microwave signatures from the same satellite, on a regional scale, for various seasons since "the physics underlying an active microwave signature may be quite different from the physics underlying a passive signature of the same piece of ice" (Hallikainen and Winebrenner, 1992).

Such an approach has already been exploited by Carsey (1985) using SEASAT sensors (SASS, SMMR) to investigate the characteristics of summer ice. Comparing SASS σ^0 to SMMR brightness temperatures, averaged over 3 days and over a 1.6 x 10^5 km^2 area, Carsey showed that SMMR data vary in the opposite way to SASS data (see Fig. 17 of his article). In the present study, this behavior has been observed along the ground tracks for the late and early winter period (thus the use of - σ^0 to ease comparisons) and can be easily understood. As explained in Hallikainen and Winebrenner (1992) : "As the strength of scattering increases, incoherently scattered intensity and thus active signatures tend to increase. However, a better scatterer typically makes a poorer absorber. According to Kirchhoff's law, the material therefore also makes a poorer emitter; as scattering increases, brightness temperatures for a given physical temperature typically decrease".

It is out of the scope of this presentation to discuss in length the physics of passive and active signatures over sea-ice. A comprehensive review of passive microwave signatures of sea-ice can be found in Eppler *et al.* (1992) and SAR and active scatterometer signatures of sea-ice are presented by Onstott (1992).

For the purpose of the present discussion about the stability of passive and active signatures with time, it must be recalled that the two frequencies of ATSR-M were selected because of their sensitivity to water vapor and liquid water to correct the sea level altimeter data for atmospheric effects. Moreover, T_b is not only a function of the surface temperature but also of ice morphology and snow layers which all are subject to seasonal variations. Eppler *et al.* (1992) distinguish five seasonal periods : winter, initial warming, melt onset, advanced melt and freeze up.

These periods can be identified on the plots of brightness temperature of Fig. 7b, where mid-April corresponds to the end of winter, then initial warming shifts the passive signature to higher T_b's (mid-May), then melt onset (June) and advance melt (July and August) occurs masking any significant signature. Then, at freeze up (October, November) a new signature shows up for the next winter period (December) blurred by oscillations of the brightness temperatures, for example between km 1200 and 1300 of Figure 6b, lower frame. It is suggested that the sea-ice has not yet stabilized and that snowfalls or atmospheric effects are the reasons for these oscillations.

The situation appears slightly different with the active microwave signature. At C band, dry snow does not contribute to backscattering which for multi-year ice is mainly governed by its structure, trapped air bubbles and brine pockets. First-year ice appears as low backscattering areas because of its smooth surface and salty upper layer.

At the end of the winter period, the initial warming does not provide enough heat to destroy the ice structure (moreover any dry snow cover acts as an insulator) and the active signature remains stable until mid-May. Analysis of σ^0 maps (not shown here) indicates that the situation did not evolve until June, 21 when melt onset changed the surface to a complex mixture of wet snow, water and melting ice.

In early fall, freeze up occurs. The new active signature appears at the beginning of October. At first glance, it seems not to stabilize rapidly since definite differences can be observed between the October, November and December signatures, for example about km 1200 (Fig. 6a bottom frame). It could be argued, as in the case of passive microwave data, that sea-ice has not yet reached its final winter structure by mid-December, but, comparing the very similar pattern of the November and December signatures, it is possible that an eastward drift of the whole ice canopy has occurred as was observed previously during late winter.

5. CONCLUSIONS

Because of its near polar orbit, the instruments on board ERS-1 sense large portions of both polar regions. Thus it has been possible to analyze collocated data from ERS-1 scatterometer and ATSR/M over the Arctic for the period from mid-April to mid-December 1992.

This analysis shows that the active signature of the scatterometer has a better dynamic range over sea-ice than the ATSR/M. The scatterometer signature which depends neither on surface temperature nor on atmospheric effects, is more stable in time as long as melting does not occur. Specifically, the initial warming period and the concomitant atmospheric contaminations which make interpretation of passive microwave data and monitoring of ice structures in late winter and early spring difficult has no (or very little) effect on the scatterometer signal. In the summer period, the signatures of both instruments are blurred by

water and wet ice surfaces. However, passive microwave data delineate the ice boundary better. In this mixed zone, ice concentration can be estimated with the ATSR/M as is the case with other single-polarization dual-frequency radiometers, but with similar limitations.

The joint analysis of data from passive and active sensors brings in new information, on a global scale, to separate the effects of different physical process. Two examples illustrate this point. First, changes in brightness temperatures observed from April to May over the Siberian area may be attributed to initial warming and atmospheric effects rather than modifications of the sea-ice structure. Second, apparent oscillations of brightness temperatures during the freeze-up and early winter periods can be separated into two consecutive and different processes : an initial phase corresponding to freeze-up followed by a sea-ice drift signature.

Because of its larger swath and its mapping capability, the SSM/I should be a better choice than the ATSR/M for joint analysis of active and passive signatures. After this first try over the Arctic with ATSR/M, we intend to investigate the use of SSM/I and the AMI-Wind data over both polar caps, orienting our investigations towards sea-ice climatology studies.

Research in other fields could take advantage of the stability of the scatterometer signature of sea-ice as long as melting does not occur. For example, it should be possible, by mixing the information from the various channels of passive microwave radiometer, to discriminate and perhaps quantify other effects which modify the brightness temperatures either along the atmospheric path, moisture for instance, or at the sea-ice surface, such as snow layer and/or surface temperature.

REFERENCES

Carsey F. D., 1985, Summer Arctic Sea-ice Character From Satellite Microwave Data. J. Geophys. Res., Vol. 90, No C3, pp. 5015-5034.

Carsey F. D., 1992, Editor, Microwave Remote Sensing of Sea-ice, Geophysical Monograph 68. American Geophysical Union.

Cavanié A. & Gohin F., 1992, Interpretation of ERS-1 Scatterometer Data over Sea-ice, in ERS-1 Geophysical Validation, Workshop Proceedings, 27-30 April 1992, Penhors, Bretagne, France. ESA wpp-36, August 1992.

Comiso J.C. & Sullivan C.W., 1986, Satellite Microwave and In Situ Observations of the Weddell Sea-ice Cover and its Marginal Ice Zone, J. Geophys. Res., Vol. 91, No C8, pp. 9663-9681, August 15.

Eppler D.T., Farmer L.D., Lohanick A.W., Anderson M.R., Cavalieri D.J., Comiso J., Gloersen P., Garrity C., Grenfell T.C., Hallikainen M., Maslanik J.A., Mätzler C., Melloh R.A., Rubinstein I. & Swift C.T., 1992, Passive Microwave Signatures of Sea-ice. In Microwave Remote Sensing of Sea-ice, pp. 47-69. F. D. Carsey Editor, Geophysical Monograph 68, American Geophysical Union.

Eymard L., Le Cornec A. & Tabary L., 1993, The ERS-1 Microwave Radiometer. Accepted for publication in Int. Jour. Remote Sensing.

Ezraty R., 1992, First Analysis of ERS-1, ATSR-M Data. Application to Antarctica. Tech. Rep. IFREMER/DRO-OS.

Ezraty R., 1993, The Computation of Ice Concentration from ATSR/M Data, Application to Antarctica. Tech. Rep. IFREMER/DRO-OS.

Gohin F. & Cavanié A., 1993, A First Try at Identification of Sea-ice Using the Three Beam Scatterometer of ERS-1. Submitted to Int. Jour. of Remote Sensing.

Hallikainen M. & Winebrenner D. P. 1992, The Physical Basis for Sea-ice Remote Sensing. In Microwave Remote Sensing of Sea-ice, pp. 29-46. F. D. Carsey Editor, Geophysical Monograph 68, American Geophysical Union.

Louet J., 1986, ERS-1 Mission Constraints Related to Wind and Wave Calibration, in ERS-1 Wind and Wave Calibration Workshop, ESA SP-262.

Onstott R.G., 1992, SAR and Scatterometer Signatures of Sea-ice. In Microwave Remote Sensing of Sea-ice, pp. 73-104. F. D. Carsey Editor, Geophysical Monograph 68, American Geophysical Union.